Applied Catalysis B: Environmental 134–135 (2013) 251–257

Contents lists available at SciVerse ScienceDirect

Applied Catalysis B: Environmental

journal homepage: www.elsevier.com/locate/apcatb

The influence of nonstoichiometry on $LaMnO_3$ perovskite for catalytic NO oxidation

Jiahao Chen [a], Meiqing Shen [a,b,*], Xinquan Wang [a], Gongshin Qi [c], Jun Wang [a], Wei Li [c,**]

[a] Key Laboratory for Green Chemical Technology of State Education Ministry, School of Chemical Engineering & Technology, Tianjin University, Tianjin 300072, PR China
[b] State Key Laboratory of Engines, Tianjin University, Tianjin 300072, PR China
[c] General Motors Global Research and Development, Chemical Sciences and Materials Systems Lab, 30500 Mound Road, Warren, MI 48090, USA

ARTICLE INFO

Article history:
Received 21 September 2012
Received in revised form
25 December 2012
Accepted 7 January 2013
Available online 26 January 2013

Keywords:
NO oxidation
Mn^{4+}/Mn^{3+} ratio
Nonstoichiometry
$LaMnO_3$ perovskite

ABSTRACT

A series of structural modified La_xMnO_3 ($x = 0.9, 0.95, 1, 1.05, 1.11$) perovskites used for NO oxidation was synthesized by a sol–gel method and characterized by XRD, BET, XPS, EPR and H_2-TPR. $La_{0.9}MnO_3$ sample exhibits superior activity, and a 50% NO conversion at 250 °C is obtained. XPS and EPR results reveal a higher Mn^{4+}/Mn^{3+} ratio in Mn-rich samples, which induce more active oxygen bonding to Mn^{4+} due to the need for balancing the chemical states and stabilizing the structure. Easily regenerated oxygen associated with Mn^{4+} catalyzes the low-temperature NO oxidation. The constant activation energy (44.8 kJ/mol) obtained in the kinetics tests indicates the same mechanism of NO oxidation operated on all the samples.

1. Introduction

Diesel and lean-burn gasoline engines have drawn wide attention due to their better fuel economy and power output [1–4]. To meet the increasingly stringent NO_x emission regulations, various catalytic conversion technologies are being developed. In these techniques, NO_2 as an intermediate species plays a key role [5–8]. NO oxidation to NO_2 is the first step in NO_x storage as implemented in lean NO_x trap (LNT) [1,3,6]. The reaction rate of selective catalytic reduction (SCR) can be substantially improved with more NO_2 in the exhaust at low temperatures (200–300 °C) [9–11]. Furthermore, NO_2 is as well used as a strong oxidizer to oxidize soot collected on a particulate filter for diesel vehicles at low temperature [4,8,12].

For such a purpose, noble metal (e.g. Pt) catalysts have been widely used for diesel exhaust after-treatment. However, the collapse of the pore structure and noble metal agglomeration (major) deactivate the catalysts easily [13,14]. More recently, perovskite type oxides have turned out to be a group of promising catalysts for NO oxidation in automotive exhaust treatment, because of their low cost, good activity and thermal stability [15].

The perovskite type oxide is generally in the formulation of ABO_3, in which the B cation coordinates with oxygen in octahedral structure, and the A cation locates in the center of the dodecahedral structure [16]. The perovskite structure is a superstructure with a ReO_3-type framework built up by the incorporation of A cation into the BO_6 octahedra. It has been reported that $LaMnO_3$ catalyst has high activity for CO oxidation [17,18], hydrocarbon combustion [19,20] and NO reduction [21]. We also have found that strontium-doped $LaMnO_3$ and $LaCoO_3$ perovskite oxides show comparable NO oxidation performance to that of a commercial platinum-based counterpart in diesel oxidation catalyst (DOC) and lean NO_x trap [22].

Compared with stoichiometric $LaMnO_3$ perovskite, nonstoichiometric ones exhibited some specific structural properties, such as change of Mn^{4+}/Mn^{3+} ratio [23], active oxygen mobility [24] and ion vacancy defect [25,26]. $LaMn_{0.9}O_3$ perovskite showed very promising activity for methane combustion due to its high surface area and defect structure [24]. Oxygen excess and cation vacancies were created for nonstoichiometric $LaMnO_3$ perovskite [27]. However, there are no reports on nonstoichiometric $LaMnO_3$ catalyst for NO oxidation reaction. Herein, the aim of this work is to investigate the effect of nonstoichiometry on the structure, chemical composition and catalytic performance of $LaMnO_3$ catalyst.

2. Experimental

2.1. Sample preparation

A series of $La_{0.9}MnO_3$ ($L_{0.9}MO$), $La_{0.95}MnO_3$ ($L_{0.95}MO$), $LaMnO_3$ (LMO), $La_{1.05}MnO_3$ ($L_{1.05}MO$) and $La_{1.11}MnO_3$ ($L_{1.11}MO$) samples

* Corresponding author at: School of Chemical Engineering and Technology, Tianjin University, 92 Weijin Road, Nankai District, Tianjin 300072, PR China.
Tel.: +86 22 27892301; fax: +86 22 27892301.
** Corresponding author. Fax: +1 586 986 8697.
E-mail addresses: mqshen@tju.edu.cn (M. Shen), wei.1.li@gm.com (W. Li).

0926-3373/$ – see front matter © 2013 Elsevier B.V. All rights reserved.
http://dx.doi.org/10.1016/j.apcatb.2013.01.027

was prepared by a citric acid sol–gel method, with metal nitrates as precursors [28]. The stoichiometric metal nitrates were dissolved together. Then, 10% (molar ratio) excess citric acid over the number of ionic equivalents of total cations was added to the aqueous solution. The solution was evaporated at 80 °C until it became viscous. The obtained sample was dehydrated at 90 °C for 12 h followed by calcination at 700 °C for 5 h in flowing air.

2.2. Characterization

The XRD patterns were acquired using a X'Pert Pro diffractometer operating at 40 kV and 40 mA with nickel-filtered Cu Kα radiation (λ = 1.5418 Å) in the range $20^\circ \leq 2\theta \leq 90^\circ$, at a 0.02° step size. The BET surface area of the samples was determined by N_2 adsorption at 77 K using the F-Sorb 3400 volumetric adsorption/desorption apparatus. Prior to the measurement, the samples were degassed at 150 °C under vacuum for 3 h. The X-ray photoelectron spectroscopy (XPS) experiments were carried out on a PHI-5300 ESCA system with Al K radiation under UHV (1.33×10^{-8} Pa). All peaks are calibrated by the carbon deposit C 1s binding energy (BE) at 284.8 eV. The atomic ratios were calculated using the atomic sensitivity factors provided by the manufacturer. Electron paramagnetic resonance (EPR) spectra were collected using X-band (ν = 9.78 GHz) EPR spectrometer (Bruker model A320) at room temperature. The magnetic field was scanned, starting from 2000 G. The *g* value was determined from precise frequency and magnetic-field values.

50 mg sample was used in each H_2 temperature programmed reduction (TPR) measurement. The sample was first oxidized by 30 ml/min O_2 at 500 °C for 30 min. And then it was cooled down to room temperature followed by purging with N_2 for 30 min. The flow of 5% H_2/N_2 (30 ml/min) was switched into the reactor afterwards. The sample was then heated up from 50 to 900 °C at a rate of 10 °C/min. The variation of H_2 concentration in the outlet gas was continually monitored by a TCD detector. In order to determine the quantitative amount of each Mn species, CuO was used to calibrate the TCD signals.

2.3. Activity test

Catalytic activity measurements for NO oxidation were carried out in a packed bed flow reactor (diameter = 6 mm; length = 36 mm). The catalysts (0.2 g) were diluted with quartz sand (1.8 g) and placed in the middle of the reactor between two clogs of quartz wool. Prior to reaction, the catalysts were pretreated by 10% O_2/N_2 (850 ml/min) at 500 °C for 1 h. After cooling to 100 °C, the gas flow was switched to 850 ml/min of 100 ppm NO, 10% O_2, 5% H_2O, 5% CO_2 and N_2 balance with gas hourly space velocity (GHSV) of 30,000 h^{-1}. The temperature increased from 100 to 450 °C at a rate of 10 °C/min. The gas concentrations were monitored (15 data points a min) by Nicolet 380 FTIR with MCT detector and 2 m gas cell.

In the NO oxidation kinetic evaluation experiment, the space velocity was selected to 432,000 h^{-1}, under which condition it has been proved to eliminate the external diffusion effect. The samples with particles of 80-100 mesh size were used in order to remove the internal diffusion effect. 25 mg (80-100 mesh) catalyst was used for each experiment to ensure the NO conversion is always lower than 20%. The samples were pretreated by 10% O_2 at 500 °C for 1 h. The steady-state NO oxidation experiments were performed using a reactant gas mixture containing 10% O_2, 300 ppm of NO with N_2 as the balance. The typical time to achieve a steady-state at each temperature was 1 h.

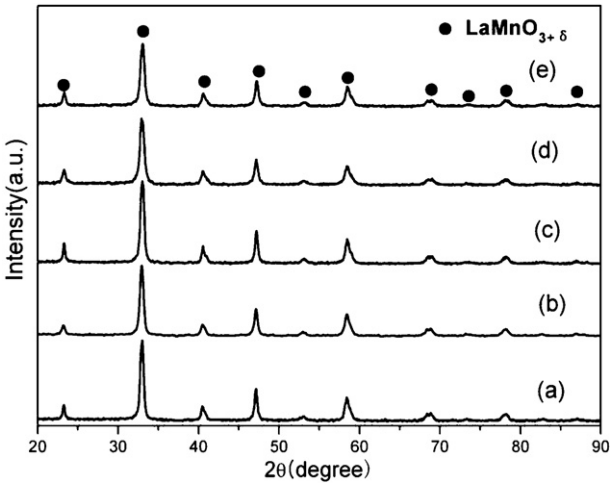

Fig. 1. XRD patterns of (a) $L_{0.9}MO$, (b) $L_{0.95}MO$, (c) LMO, (d) $L_{1.05}MO$ and (e) $L_{1.11}MO$ samples.

3. Results and discussions

3.1. XRD and BET

Fig. 1 shows the XRD patterns of La_xMnO_3 (x = 0.9, 0.95, 1, 1.05, 1.11) samples. Single phase was obtained for all the samples. No segregated phases of lanthanum oxide or manganese oxide were detected. The orthorhombic structure of $L_{0.9}MO$ and $L_{0.95}MO$ was generated. And the rhombohedral structure of the others was obtained. The unit cell volume increased with increasing La/Mn ratio. The increase of the cell volume may be due to the transformation of Mn^{4+} (ionic radius = 0.540 Å) into larger radius Mn^{3+} (ionic radius = 0.645 Å) cation in the structure [29,30]. Meanwhile, the oxygen content decreased in accordance with the reduction of Mn^{4+} content. Furthermore, the unit cell expanded as the oxygen content decreased [31]. The average crystal size within these particles slightly decreases with increasing La/Mn ratio as shown in Table 1. The surface area of these samples varies between 14.5 m^2/g ($L_{1.11}MO$) and 23.1 m^2/g ($L_{0.9}MO$).

3.2. XPS

The surface atom composition calculated using sensitivity atomic factors took place by XPS analyses detecting the binding energies. The Mn 2p and O 1s peaks of La_xMnO_3 (x = 0.9, 0.95, 1, 1.05, 1.11) samples are displayed in Figs. 2 and 3. For Mn 2p spectrum in Fig. 2, peak intensities were evaluated by applying a peak synthesis procedure that includes three components of Mn^{4+}, Mn^{3+} and a satellite. It is ambiguous in the recognition of the Mn^{4+} and Mn^{3+} species. Because the differences between the binding energy values of Mn^{3+} and Mn^{4+} ions were very small. The components close to 642.4 eV (Mn^{4+}) and 641.3 eV (Mn^{3+}) were observed for all the samples [16,32]. The satellite peak (644.2 eV) of the Mn $2p_{3/2}$ level was weak in all the samples in comparison with that of Mn^{3+} and Mn^{4+} peaks. The Mn^{4+}/Mn^{3+} atomic ratio is summarized in Table 2. Apparently, the concentration of Mn^{4+} decreased, while the Mn^{3+} content exhibited a contrary trend. Partial oxidation of Mn^{3+} into Mn^{4+} ions on the surfaces of the catalysts gave rise to the formation of structural defects. The enhanced mobility of oxygen from the crystal lattice of the perovskite resulted in an increased catalyst activity [18]. Therefore, with lower La content in La-Mn-O perovskite, excess Mn sites and increasing surface Mn^{4+} were achieved [33].

The O 1s spectrum was shown in Fig. 3. There were three oxygen signals located at 529.3–529.9, 531.0–531.4 and 533 eV

Table 1
Lattice parameter and surface area of the La_xMnO_3 (x = 0.9, 0.95, 1, 1.05, 1.11) samples.

Sample	Symmetry	a (Å)*	b (Å)*	c (Å)*	V (Å^3)*	D (nm)*	S_{BET} (m^2/g)
$L_{0.9}MO$	Orthorhombic	5.479	5.433	7.698	229.15	22.9	23.1
$L_{0.95}MO$	Orthorhombic	5.490	5.528	7.788	236.33	27.6	15.4
LMO	Rhombohedral	5.465	5.465	13.242	342.46	23.4	19.5
$L_{1.05}MO$	Rhombohedral	5.465	5.465	13.232	342.26	20.5	17.5
$L_{1.11}MO$	Rhombohedral	5.471	5.471	13.255	343.57	19.0	14.5

* The error of the data calculated by Jade 5.0 was less than 6%.

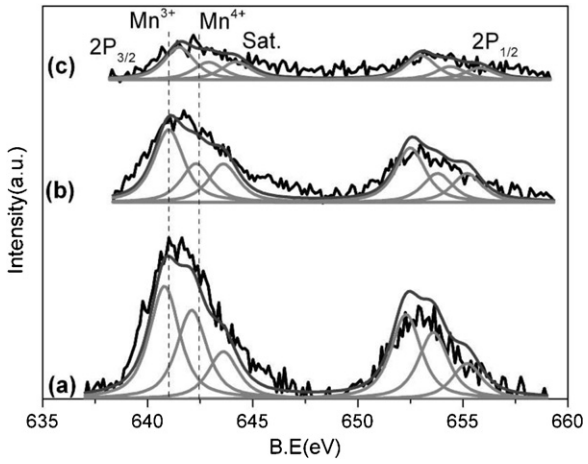

Fig. 2. XPS spectra of Mn 2p for (a) $L_{0.9}MO$, (b) LMO and (c) $L_{1.11}MO$ samples.

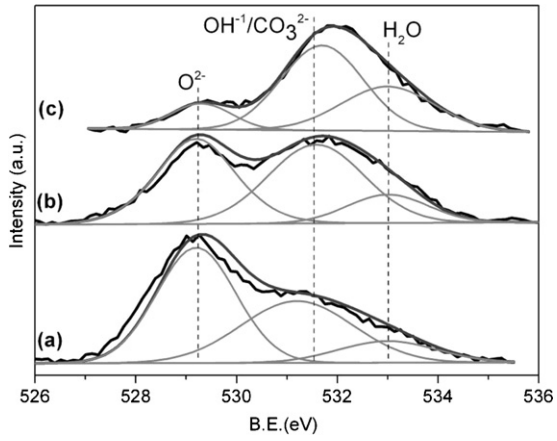

Fig. 3. XPS spectra of O 1s for (a) $L_{0.9}MO$, (b) LMO and (c) $L_{1.11}MO$ samples.

Table 2
Mn 2p and O 1s binding energy and surface atomic ratio of the La_xMnO_3 (x = 0.9, 0.95, 1, 1.05, 1.11) samples.

Sample	Mn 2p	Mn^{4+}/Mn^{3+}	O 1s	O_{latt}/O_{total}
$L_{0.9}MO$	640.8	0.79	529.2	0.59
	642.1		531.2	
	643.6		533.0	
$L_{0.95}MO$	641.2	0.71	529.2	0.38
	642.5		531.6	
	644.2		533.0	
LMO	641.2	0.64	529.2	0.36
	642.5		531.6	
	644.1		533.0	
$L_{1.05}MO$	641.1	0.58	529.2	0.35
	642.4		531.7	
	644.1		533.0	
$L_{1.11}MO$	641.5	0.54	529.3	0.12
	642.9		531.7	
	644.2		533.0	

attributed to lattice oxygen O_{latt} (O^{2-}), hydroxyl and/or carbonate species and adsorbed molecular water, respectively [16,34]. The molar ratio of O_{latt}/O_{total} was obtained by quantitative calculation of the corresponding peaks areas and is shown in Table 2. The trend of O_{latt}/O_{total} molar ratio follows the same sequence as that of Mn^{4+}/Mn^{3+} molar ratio. Moreover, the $L_{0.9}MO$ sample not only exhibits the highest Mn^{4+}/Mn^{3+} molar ratio, but also possesses the highest O_{latt}/O_{total} molar ratio among all the samples. The lattice oxygen content was in agreement with the result of Mn^{4+} content obtained by H_2-TPR and EPR. Hence, it is indicated that the Mn^{4+} ion with oxygen complexing plays the key role in NO oxidation reaction over La_xMnO_3 perovskites.

3.3. EPR

Both Mn^{2+} and Mn^{4+} ions give EPR signals, but Mn^{3+} ion is EPR silent due to its large zero-field splitting [35]. The Mn^{2+} ion is excluded from the La-Mn-O perovskites according to the XPS results. The EPR spectrum of Mn^{4+} ion is ascribed to its electron configuration in an octahedral field ($^4A_{2g}$). And the g factor is determined by the free electron and the zero field splitting [36]. In the case of the manganites, the g factor is almost temperature independent and equal to the free electron value. In contrast, the linewidths show a wide variety of behaviors depending on both the temperature and concentration of ions. In addition, the linewidth increased with decreasing Mn^{4+} content in the $La_{1-x}A_xMnO_3$ (A = Ca, Sr) perovskites [37]. The EPR spectra of Mn^{4+} ion are presented in Fig. 4. The linewidth (ΔH) and g factor of the samples are displayed in Table 3. Obviously, the linewidth increased with increasing x value (La/Mn ratio). The intensity of the signal was also weakened with increasing La/Mn ratio. Therefore, the concentration of Mn^{4+} in the bulk of La_xMnO_3 (x = 0.9, 0.95, 1, 1.05, 1.11) perovskites decreased with higher La/Mn ratio.

The role of Mn^{4+} in oxidation reaction has been investigated in many reports. Giannakas et al. indicated that more amount of Mn^{4+} can promote the conversion of NO and CO reaction [38]. Zhang and his co-workers found that more Mn^{4+} content enhanced

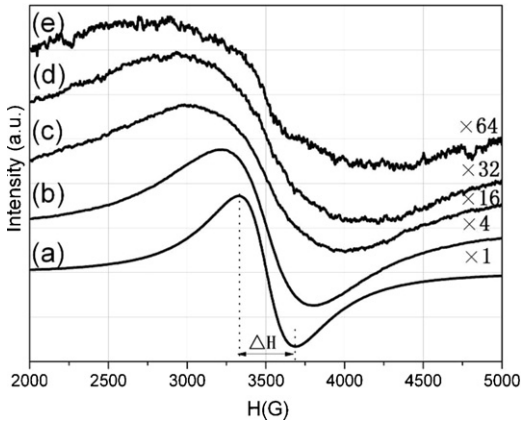

Fig. 4. EPR spectra of (a) $L_{0.9}MO$, (b) $L_{0.95}MO$, (c) LMO, (d) $L_{1.05}MO$ and (e) $L_{1.11}MO$ samples.

Table 3
Linewidth (ΔH) and g value of the La_xMnO_3 (x = 0.9, 0.95, 1, 1.05, 1.11) samples.

Sample	ΔH (G)	g value
$L_{0.9}MO$	358	1.9920
$L_{0.95}MO$	578	1.9923
LMO	1024	1.9936
$L_{1.05}MO$	1270	1.9924
$L_{1.11}MO$	1438	1.9991

the catalytic oxidation of vinyl chloride emission by part substitution of Mn with Co, Fe and Ni [39]. More amount of manganese shifted from a III to a IV oxidation state may promote an increase in the catalytic activity, owing to the enabled possibility of the lattice oxygen close to Mn^{4+} to be easily reacted away by methane [40]. The intrinsic reason why Mn^{4+} content correlates well with the oxidation activity is that the reaction mechanism likely needs Mn^{4+}/Mn^{3+} pairs. Thus, the more active site pairs are obtained with more Mn^{4+} content. Therefore, the increasing Mn^{4+} ratio generated by nostoichiometry can be resulted in higher NO oxidation activity.

3.4. H_2-TPR

TPR experiment is a useful method to investigate the reducible oxygen species of the perovskite catalysts. Since NO oxidation reaction is a redox procedure, the transformation of B type metal ion between Mn^{3+} and Mn^{4+} states of $LaMnO_3$ catalyst is supposed to be involved [24]. The H_2-TPR profiles of La_xMnO_3 (x = 0.9, 0.95, 1, 1.05, 1.11) samples are showed in Fig. 5. The samples exhibited two major H_2 consumption peaks. The first peak is located at 340 °C and the other is positioned at 820 °C. It is suggested that this process is a multiple-step reduction. Herein, in order to determine the reduction species, take the LMO sample for instance. It was reduced at different temperatures and then collected the EPR signal. The reduction temperatures include 220 °C, 300 °C, 550 °C and 850 °C. The EPR spectra of LMO sample reduced at different temperatures are presented in Fig. 6. And the results of g factor and linewidth (ΔH) are displayed in Table 4.

There was no change of the linewidth (ΔH) between the unreduced sample and that reduced at 220 °C for 30 min. Besides, the perovskite structure retained well. In other words, the reduced species was surface oxygen. The reduction of this species did not change the valence state of Mn ion. When the LMO sample was reduced at 300 °C, the linewidth (ΔH) increased from 1024 G to 1796 G. It means that the Mn^{4+} content was reduced.

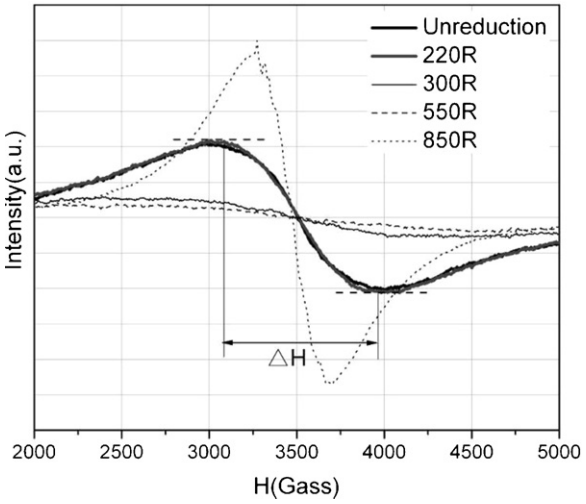

Fig. 6. EPR spectra of LMO sample reduced at different temperature.

Table 4
Linewidth (ΔH) and g value of LMO sample pretreated at different reduction conditions.

Sample	Unreduction	220R	300R	550R	850R
g value	1.9936	1.9948	1.9983	1.9868	2.0001
ΔH (G)	1024	1043	1796	2239	428

Furthermore, the linewidth of LMO sample reduced at 550 °C rose up to 2239 G. Obviously, it is indicated that the Mn^{4+} content was further reduced.

The linewidth decreased to 428 G and the intensity increased for the LMO sample reduced at 850 °C. This was ascribed to the generation of MnO phase decomposed from LMO perovskite as shown in Fig. 7. The hyperfine line of Mn^{2+} EPR spectroscopy was clearly exhibited due to the hyperfine structure of MnO, at g = 2.0001 [41]. Thus, if the reduction of Mn^{3+} to Mn^{2+} occurs when LMO is reduced at 550 °C, the intensity will increase and the linewidth will decrease. However, the experimental results indicate that the intensity decreased and the linewidth increased after the reduction of LMO at 550 °C.

Based on the above results, it is can be concluded that the reduction peaks below 550 °C are ascribed to the reduction of Mn^{4+} to Mn^{3+} and the reduction of surface oxygen. There is no the

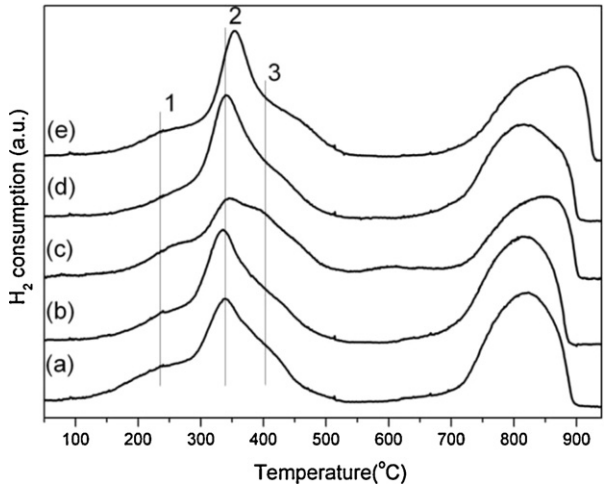

Fig. 5. H_2-TPR profiles of (a) $L_{0.9}MO$, (b) $L_{0.95}MO$, (c) LMO, (d) $L_{1.05}MO$ and (e) $L_{1.11}MO$ samples.

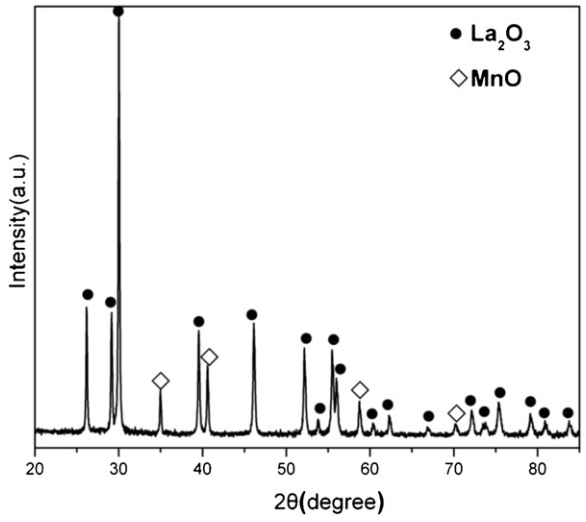

Fig. 7. XRD pattern of LMO sample reduced at 850 °C for 30 min.

Table 5
Quantitative results of reduction species in the La_xMnO_3 (x = 0.9, 0.95, 1, 1.05, 1.11) samples.

Sample	H_2 consumption (μmol)			
	220-230 °C	330-340 °C	370-380 °C	330-380 °C
$L_{0.9}MO$	7.6	11.6	44.1	55.8
$L_{0.95}MO$	6.6	12.6	34.0	46.6
LMO	10.1	26.9	16.4	43.3
$L_{1.05}MO$	10.8	18.6	21.6	40.2
$L_{1.11}MO$	8.9	7.6	21.5	29.1

reduction of Mn^{3+} to Mn^{2+}. The peak area of the La_xMnO_3 (x = 0.9, 0.95, 1, 1.05, 1.11) samples was showed in Table 5. The peak area located at 330-380 °C decreased with increasing x value. It is indicated that the Mn^{4+} content decreased with higher La/Mn ratio. This trend is in accord with the EPR results.

3.5. Catalytic activity

Fig. 8 shows the NO conversion of La_xMnO_3 (x = 0.9, 0.95, 1, 1.05, 1.11) catalysts. The activity of $L_{0.9}MO$ sample, showing the maximum conversion of 85% at 296 °C, is much higher than that of LMO sample. The catalytic performance is in the order of $L_{0.9}MO > L_{0.95}MO > LMO \approx L_{1.05}MO > L_{1.11}MO$.

In the $LaMnO_3$ perovskite, La sites are the inert components for NO oxidation reaction. The active sites should be ascribed to Mn and oxygen, which is due to their redox ability. The higher Mn oxidation state could promote redox ability. Mn is partially reduced by providing the reaction oxygen. And then the reduced Mn is reoxidized by oxygen from the gas phase [42]. The unstable oxidation states of Mn^{4+} and Mn^{3+} have been considered the main origins of the $LaMnO_{3+\delta}$ activity [43]. In terms of the Mn^{4+} oxygen vacancy, in a stoichiometric $LaMnO_3$, all the Mn should be Mn^{3+}. When we decrease the La/Mn ratio, some of the La sites will be empty and in order to maintain the charge neutrality, the Mn^{4+} increases together with oxygen vacancies. The oxygen filling these vacancy sites will be less stable compared to normal lattice oxygen coordinated to Mn^{3+}. Hence, perovskite with vacancy is more active for oxidation reactions with lower apparent oxygen activation energy [44]. In our present work, with the decrease of La/Mn ratio, the evolution of Mn^{4+} contents calculated by EPR and the trend of lattice oxygen contents calculated by XPS and H_2-TPR in La_xMnO_3 (x = 0.9, 0.95, 1, 1.05, 1.11) perovskites are proportional to NO oxidation activity, respectively. In other words, it means that the amount of Mn^{4+} associated with lattice oxygen has the same trend with NO oxidation activity. Hence, it can be inferred that the Mn^{4+} ion with lattice oxygen plays the key role in the oxidation of NO over La_xMnO_3 perovskites.

To further investigate the role of Mn^{4+} and active oxygen, the most active $L_{0.9}MO$ sample was taken for instance. It was reduced at different temperatures under 5% H_2 for 5 min to reduce the amount of Mn^{4+} and associated oxygen species. Below 550 °C, the amount of Mn^{4+} and oxygen decreased under reduction condition as described above. Consequently, the Mn^{4+}/Mn^{3+} ratio decreases when the sample is reduced at the temperature between 250 and 550 °C. The NO conversion profile of $L_{0.9}MO$ reduced at 200 °C, 330 °C and 500 °C is presented in Fig. 9. It is obviously observed that there is no deactivation for $L_{0.9}MO$ sample after reduction at 200 °C. This result indicates that surface oxygen species may not play an important role in NO oxidation process. Another possibility is that surface oxygen can be regenerated under oxidation condition. When $L_{0.9}MO$ sample was reduced at 330 °C and 500 °C, the sharp decrease of NO oxidation performance below 300 °C was observed. What's more, the activity of $L_{0.9}MO$ sample reduced at 500 °C was apparently lower than that reduced at 330 °C. This result clearly suggests that the Mn^{4+} ion with oxygen complexing play the key role in NO oxidation reaction over La-Mn-O perovskites.

The apparent activation energy determined in the temperature range of 200–275 °C is 44.8 ± 2.7 kJ/mol as shown in Fig. 10. The similarity of the activation energy values among these catalysts suggests that the mechanism of NO oxidation over the La_xMnO_3 (x = 0.9, 0.95, 1, 1.05, 1.11) catalysts is the same. The higher rate of NO conversion indicates more active sites accompanying with more amount of Mn^{4+} associated with O ligand. The linewidth (ΔH) verifies the correlation between the NO oxidation activity and Mn^{4+} associated with O ligand.

The role of Mn^{4+} associated with O ligand can be explained by the structural stability. The higher La/Mn ratio results in the decreasing Mn^{4+} content. It has been argued that the charge defect caused by La vacancy is compensated by the oxidation of Mn^{3+} into Mn^{4+} rather than by the creation of oxygen vacancy [27]. Conversely, excess La in A site results in less Mn^{4+} content to balance the charge neutralization. The perovskites with less La in A site are most likely to coordinate with less stable local structure. Therefore, the catalyst is more active with more active sites of Mn^{4+} ion associated with O ligand. Besides that, this can be explained by

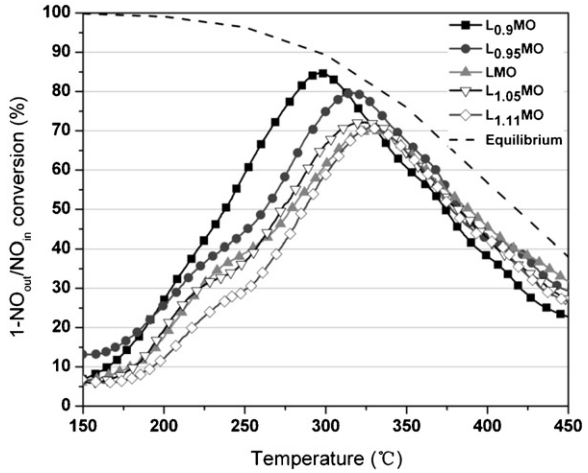

Fig. 8. Catalytic activity of $1 - NO_{out}/NO_{in}$ conversion of the La_xMnO_3 (x = 0.9, 0.95, 1, 1.05, 1.11) samples (inlet gas: 100 ppm NO, 10% O_2, 5% H_2O, 5% CO_2, N_2 balance; GHSV = 30,000 h^{-1}).

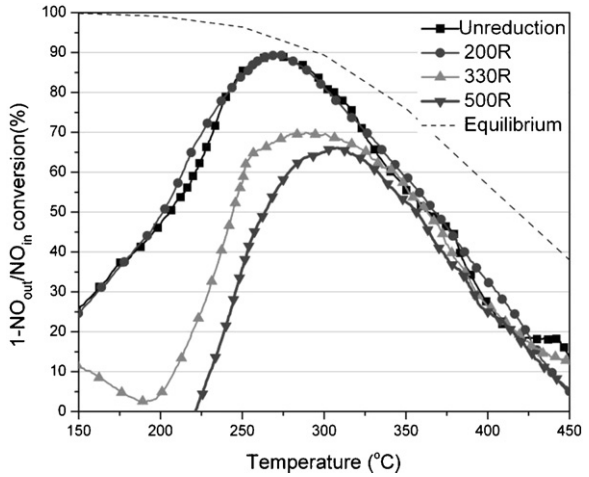

Fig. 9. $1 - NO_{out}/NO_{in}$ conversion profile of $L_{0.9}MO$ sample reduced at 200 °C (●), 330 °C (▲) and 500 °C (▼) respectively (evaluation condition: 100 ppm NO, 10% O_2, N_2 balance, 1.8 g quartz + 0.2 g catalyst, GHSV = 30,000 h^{-1}; oxidation condition: 850 ml/min 10% O_2/N_2 for 1 h at the target temperature; reduction condition: 60 ml/min 5% H_2 for 5 min at the target temperature).

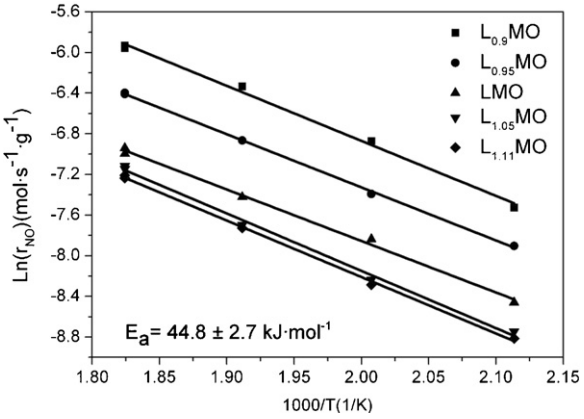

Fig. 10. Arrhenius plots for the La_xMnO_3 (x = 0.9, 0.95, 1, 1.05, 1.11) catalysts in the temperature range of 200–275 °C, showing negligible change in apparent activation energy.

the 18 electron rule. The 18e principle corresponds for 3d metals to a krypton-like electronic structure $(ns)^2(np)^6((n-1)d)^{10}(n=4)$ [45]. The O/Mn atomic ratio equals three and each Mn ion coordinates with three oxygen atoms in every structure cell. The valence shell of Mn^{3+} in the formation of $(MnO_3)^{2-}$ localized in the MnO_6 octahedron consists of nine valence orbitals. These valence orbitals collectively accommodate 18 electrons either as nonbonding electron pairs or as bonding electron pairs [46]. The $(MnO_3)^{2-}$ complex with 18 valence electron is very stable. This structural stability decreases when part of the Mn^{3+} is replaced by Mn^{4+} in the complex.

In terms of the reaction mechanism, there is no report about the NO oxidation mechanism over $LaMnO_3$ perovskite. The Mars Van Krevelen mechanism proposes that the reactant is oxidized by lattice oxide ions at the catalyst surface. The function of gas-phase oxygen is to replenish the reduced sites by adsorption and solid-state diffusion [47]. Royer et al. suggested that the CH_4 oxidation reaction over $LaCoO_3$ perovskite was followed the Mars Van Krevelen mechanism [48]. Petrolekas et al. indicated that the mechanism of CO oxidation over $La_{0.5}Sr_{0.5}MnO_{3+\delta}$ perovskite was the Mars Van Krevelen mechanism at 500 °C [49]. According to our present data, it is indicated that the content of Mn^{4+} associated with O correlates well with the NO oxidation performance. We know that it is the oxygen species near Mn^{4+} that is active for NO oxidation.

4. Conclusions

Stoichiometric and nonstoichiometric La-Mn-O perovskites were prepared by the sol–gel method. The single phase was detected in each sample without segregated phases. The nonstoichiometric $La_{0.9}MnO_3$ sample exhibits the best activity of NO oxidation. The lower La content in A site induces the transformation of Mn^{3+} into Mn^{4+} for charge balance and structural stability. The amount of Mn^{4+} associated with O ligand is in agreement with the activity of NO oxidation. The same mechanism of NO oxidation over the La-Mn-O perovskites is observed. The oxygen species associated with modified Mn^{4+}/Mn^{3+} sites of the La-Mn-O perovskites catalyzes the low temperature NO oxidation.

Acknowledgements

The authors would like to acknowledge the GM Global Research & Development (RD-07-312-NV487) for the financial support of the project. This work was also supported by the National High Technology Research and Development Program of China (863 Program, 2011AA03A405).

Appendix A. Supplementary data

Supplementary data associated with this article can be found, in the online version, at http://dx.doi.org/10.1016/j.apcatb.2013.01.027.

References

[1] X. Auvray, T. Pingel, E. Olsson, L. Olsson, Applied Catalysis B 129 (2013) 517–527.
[2] J.R. Theis, E. Gulari, Applied Catalysis B 74 (2007) 40–52.
[3] M. Kaneeda, H. Iizuka, T. Hiratsuka, N. Shinotsuka, M. Arai, Applied Catalysis B 90 (2009) 564–569.
[4] K. Leistner, A. Nicolle, P.D. Costa, Applied Catalysis B 111–112 (2012) 415–423.
[5] A. Boubnov, S. Dahl, E. Johnson, A.P. Molina, S.B. Simonsen, F.M. Cano, S. Helveg, L.J.L. Yegres, J.D. Grunwaldtd, Applied Catalysis B 126 (2012) 315–325.
[6] W. Hauptmann, M. Votsmeier, J. Gieshoff, A. Drochner, H. Vogel, Applied Catalysis B 93 (2009) 22–29.
[7] L.D. Li, L.L. Qu, J. Cheng, J.J. Li, Z.P. Hao, Applied Catalysis B 88 (2009) 224–231.
[8] J. Després, M. Elsener, M. Koebel, O. Kröcher, B. Schnyder, A. Wokaun, Applied Catalysis B 50 (2004) 73–82.
[9] K. Krishna, A.B. López, M. Makkee, J.A. Moulijn, Applied Catalysis B 75 (2007) 201–209.
[10] M.F. Irfan, J.H. Goo, S.D. Kim, Applied Catalysis B 78 (2008) 267–274.
[11] K. Hauff, H. Dubbe, U. Tuttlies, G. Eigenberger, U. Nieken, Applied Catalysis B 129 (2013) 273–281.
[12] L. Capek, L. Vradman, P. Sazama, M. Herskowitz, B. Wichterlova, R. Zukerman, R. Brosius, J.A. Martens, Applied Catalysis B 70 (2007) 53–57.
[13] D.M. Fernandes, C.F. Scofield, A.A. Neto, M.J.B. Cardoso, F.M.Z. Zotin, Chemical Engineering Journal 160 (2010) 85–92.
[14] D.H. Kim, Y.H. Chin, G.G. Muntean, A. Yezeretz, N.W. Currier, W.S. Epling, H.Y. Chen, H. Hess, C.H.F. Peden, Industrial and Engineering Chemistry Research 45 (2006) 8815–8821.
[15] H.Z. Azad, A. Khodadadi, P.E. Ahranjani, Y. Mortazavi, Applied Catalysis B 102 (2011) 62–70.
[16] S. Ponce, M.A. Peña, J.L.G. Fierro, Applied Catalysis B 24 (2000) 193–205.
[17] Y.Z. Steenwinkel, L.M. van der Zande, H.L. Castricum, A. Bliek, Applied Catalysis B 54 (2004) 93–103.
[18] B. Kucharczyk, W. Tylus, Applied Catalysis A 335 (2008) 28–36.
[19] P.E. Ahranjani, A. Khodadadi, H.Z. Azad, Y. Mortazavi, Chemical Engineering Journal 169 (2011) 282–289.
[20] S. Cimino, L. Lisi, S. De Rossi, M. Faticanti, P. Porta, Applied Catalysis B 43 (2003) 397–406.
[21] R.D. Zhang, A. Villanueva, H. Alamdari, S. Kaliaguine, Journal of Molecular Catalysis A 258 (2006) 22–34.
[22] C.H. Kim, G.S. Qi, K. Dahlberg, W. Li, Science 327 (2010) 1624–1627.
[23] H. Vincent, M. Audier, S. Pignard, G. Dezanneau, J.P. SeHnateur, Journal of Solid State Chemistry 164 (2002) 177–187.
[24] R. Spinicci, A. Delmastro, S. Ronchetti, A. Tofanari, Materials Chemistry and Physics 78 (2002) 393–399.
[25] M. Wolcyrz, R. Horyn, F. Boure, E. Bukowska, Journal of Alloys and Compounds 353 (2003) 170–174.
[26] J.A. Alonso, M.J. Martínez-Lope, M.T. Casais, J.L. MacManus-Driscoll, P.S.I.P.N. de Silva, L.F. Cohen, M.T. Fernández-Díaz, Journal of Materials Chemistry 7 (1997) 2139–2144.
[27] G. Dezanneau, A. Sin, H. Roussel, M. Audier, H. Vincent, Journal of Solid State Chemistry 173 (2003) 216–226.
[28] E. Arendt, A. Maione, A. Klisinska, O. Sanz, M. Montes, S. Suarez, J. Blanco, P. Ruiz, Applied Catalysis A 339 (2008) 1–14.
[29] M.B. Bellakki, C. Shivakumara, N.Y. Vasanthacharya, A.S. Prakash, Materials Research Bulletin 45 (2010) 1685–1691.
[30] J.A.M. van Roosmalen, P. van Vlaanderen, E.H.P. Cordfunke, W.L. Ijdo, D.J. Ijdo, Journal of Solid State Chemistry 114 (1995) 516–523.
[31] S. Miyoshi, A. Kaimai, H. Matsumoto, K. Yashiro, Y. Nigara, T. Kawada, J. Mizusaki, Solid State Ionics 175 (2004) 383–386.
[32] Y.N. Lee, R.M. Lago, J.L.G. Fierro, J. Gonzaez, Applied Catalysis A 215 (2001) 245–256.
[33] V. Ferris, G. Goglio, L. Brohan, O. Joubert, P. Molinie, M. Ganne, P. Dordor, Materials Research Bulletin 32 (1997) 763–777.
[34] H. Najjar, J.-F. Lamonier, O. Mentré, J.-M. Giraudon, H. Batis, Applied Catalysis B 106 (2011) 149–159.
[35] T. Li, Y.D. Li, Industrial and Engineering Chemistry Research 47 (2008) 1404–1408.
[36] R. Stoyanova, M. Gorova, E. Zhecheva, Journal of Physics and Chemistry of Solids 61 (2000) 615–620.
[37] D.L. Huber, G. Alejandro, A. Caneiro, M.T. Causa, F. Prado, M. Tovar, S.B. Oseroff, Physical Review B 60 (1999) 12155–12161.
[38] A.E. Giannakas, A.K. Ladavos, P.J. Pomonis, Applied Catalysis B 49 (2004) 147–158.
[39] C.H. Zhang, C. Wang, W.C. Zhan, Y.L. Guo, Y. Guo, G.Z. Lu, A. Baylet, A.G. Fendlerb, Applied Catalysis B 129 (2013) 509–516.
[40] G. Saracco, F. Geobaldo, G. Baldi, Applied Catalysis B 20 (1999) 277–288.
[41] M. Mazur, M. Kleinova, J. Moncol, P. Stachova, M. Valko, J. Telser, Journal of Non-Crystalline Solids 352 (2006) 3158–3165.

[42] J.G. Deng, L. Zhang, H.X. Dai, H. He, C.T. Au, Journal of Molecular Catalysis A 299 (2009) 60–67.
[43] F. Teng, W. Han, S.H. Liang, B. Gaugeu, R.R. Zong, Y.F. Zhu, Journal of Catalysis 250 (2007) 1–11.
[44] N. Lakshminarayanan, H. Choi, J.N. Kuhn, U.S. Ozkan, Applied Catalysis B 103 (2011) 318–325.
[45] P. Pyykkö, Journal of Organometallic Chemistry 691 (2006) 4336–4340.
[46] G.J. Zhou, in: L. He, X. Zhao (Eds.), Advanced Inorganic Chemistry, Science Press, Beijing, 2011, pp. 257–263 (Chapter 7).
[47] A.M. Ali, E.A.C. Emanuelsson, D.A. Patterson, Applied Catalysis B 97 (2010) 168–181.
[48] S. Royer, H. Alamdari, D. Duprez, S. Kaliaguine, Applied Catalysis B 58 (2005) 273–288.
[49] P.D. Petrolekas, I.S. Metcalfe, Journal of Catalysis 152 (1995) 147–163.